

Active flow control for drag reduction through multi-agent reinforcement learning on a turbulent cylinder at $Re_D = 3900$

Pol Suárez^{1*}, Francisco Álcantara-Ávila¹, Arnau Miró², Jean Rabault³, Bernat Font⁴, Oriol Lehmkuhl², Ricardo Vinuesa^{1*}

¹FLOW, Engineering Mechanics, KTH Royal Institute of Technology, Stockholm, SE-100 44, Sweden.

²Barcelona Supercomputing Center (BSC-CNS), Barcelona, 08034, Spain.

³Independent Researcher, Oslo, Norway.

⁴Faculty of Mechanical Engineering, Technische Universiteit Delft, Delft, 2600 AA, The Netherlands.

*Corresponding author(s). E-mail(s): polism@kth.se;
rvinuesa@mech.kth.se;

Abstract

This study presents novel active-flow-control (AFC) strategies aimed at achieving drag reduction for a three-dimensional cylinder immersed in a flow at a Reynolds number based on freestream velocity and cylinder diameter of $Re_D = 3900$. The cylinder in this subcritical flow regime has been extensively studied in the literature and is considered a classic case of turbulent flow arising from a bluff body. The strategies presented are explored through the use of deep reinforcement learning. The cylinder is equipped with 10 independent zero-net-mass-flux jet pairs, distributed on the top and bottom surfaces, which define the AFC setup. The method is based on the coupling between a computational-fluid-dynamics solver and a multi-agent reinforcement-learning (MARL) framework using the proximal-policy-optimization algorithm. Thanks to the acceleration in training facilitated by exploiting the local invariants with MARL, a drag reduction of 8% was achieved, with a mass cost efficiency two orders of magnitude lower than those of the existing classical controls in the literature. This development represents a significant advancement in active flow control, particularly in turbulent regimes critical to industrial applications.

Keywords: Fluid mechanics, Drag reduction, Deep learning, Active flow control, Multi-agent reinforcement learning

1 Introduction

Active-flow-control (AFC) devices are essential tools across diverse industries, aiming at optimizing fluid-flow processes, enhancing performance, and improving overall efficiency [1]. Currently, the aeronautical sector is in need of more robust and sophisticated systems to develop better control strategies. In this scenario, innovative solutions are required to address the pressing environmental concerns linked to fossil-fuel dependence. Discovering and understanding physical mechanisms to reduce air resistance is crucial for the sustainable development of the transport industry. Passive-flow-control (PFC) solutions, while simpler and easier to integrate, typically lack the adaptability and performance capabilities of AFC methods. However, in critical sectors like aerospace, automotive, energy, and maritime, AFC devices emerge as pivotal tools, effectively managing airflow around surfaces, minimizing drag, boosting lift, and controlling separation. For instance, some passive systems are protuberances or fixed flaps such as vortex generators or winglets. On the other hand, active devices like slats and flaps which are placed along the airplane wings enhance maneuverability and efficiency. Optimizing all these devices is challenging due to the complex interactions between pressure and viscous effects across multiple flight conditions. In order to design and converge to possible solutions, substantial experience and computational resources are required.

Recent advancements in flow control have been complemented by the integration of machine-learning (ML) techniques, offering significant promise to the aeronautics sector. This includes the exploration of fundamental issues in fluid mechanics [2] and the development of novel approaches for both active and passive flow control (AFC and PFC) [3]. Deep reinforcement learning (DRL), particularly, has emerged as a rapidly expanding field within ML, capturing substantial interest. Following its success in domains like board games [4] and robotics [5], DRL demonstrates effectiveness in systems where a controller interacts with an environment to optimize a particular task; note that this is a characteristic highly relevant to many AFC scenarios. In such instances, DRL can dynamically interact with the flow, receiving feedback and refining actions iteratively over time. Designing AFC setups involves grappling with complex, high-dimensional systems, requiring significant computational power to explore the vast parameter space and identify optimal values. DRL and neural networks streamline this process, facilitating the development of effective control strategies with a reduced computational burden.

The state-of-the-art on DRL for AFC applications is rapidly expanding, featuring studies on flow control for two-dimensional (2D) cylinders across a range of Re_D (Reynolds number based on inflow velocity U_∞ and cylinder diameter D) from 100 to 8000, resulting in drag reductions of 17% and 33%, respectively [6–10]. Specific studies

have also focused on the mitigation of vortex-induced vibrations, *e.g.* [11]. Additionally, research on the application of DRL has been conducted on aircraft wings [12], fluid-structure interaction [11], and controlling highly turbulent flows, as demonstrated in Ref. [13], successfully reducing a turbulent separation bubble at a friction Reynolds number of $Re_\tau = 750$. There are studies focused on flow control in turbulent channels [14] and Rayleigh–Bénard convection [15]. Recent literature also suggests the possibility of transfer learning from 2D cylinders to three-dimensional (3D) domains and higher Re_D [16]. Recent research [17], has pushed the boundaries of current 3D cylinder state-of-the-art. This advancement involves DRL training directly in 3D, considering Reynolds numbers that include the transition to three-dimensional wake instabilities ($Re_D = 100$ to 400). The latter utilized an AFC configuration comprising numerous zero-net-mass-flow (ZNMF) actuators managed through a multi-agent reinforcement-learning (MARL) framework.

The present work aims to build upon previous successful training in transition regimes, pushing further to address the significant challenge of reaching a subcritical Reynolds number of $Re_D = 3900$. Facing a more complex scenario to explore and more intricate structures to learn from. This classic case has been extensively investigated [18–23], serving as a reference for benchmarking and facilitating the study of well-known physics. Such insights are very valuable for devising an appropriate closed-loop control mechanism within a MARL framework. Despite the wealth of documentation available, consisting of numerous simulations and experiments, there remains a degree of inconsistency when comparing the time-averaged statistics in the near-cylinder wake. This inconsistency primarily stems from the high sensitivity to minor disturbances and the unsteady behavior of vortex formation, which directly impacts the configuration of the near wake. The primary point of discussion revolves around determining the number of shedding cycles required to attain converged statistics. Recent studies demonstrate how the presence of low-frequency fluctuation mechanisms, along with the well-established vortex-shedding frequency and smaller Kelvin–Helmholtz instabilities, contribute to the gradual contraction and expansion of the recirculation region [18].

We first considered a control periodic in time and uniform in the spanwise direction as a baseline. We identified the optimal frequency of actuation around the vortex-shedding frequency f_{vs} , and also adjusted the maximum amplitude. Although this strategy led to drag reduction for Re_D between 100 to 400 [17], at the present Reynolds number of 3900 this approach actually increased the drag by 30 to 50%.

Kim & Choi (2005) [24] studied flow-control strategies for the 3D cylinder at $Re_D = 3900$, and reported successful drag reduction control by considering two types of control: In-phase and Out-of-phase. In their control strategies they consider sinusoidal profiles in the spanwise direction of the cylinder, but fixed blowing and suction constant in time. The velocity profile consists of a constant normal velocity of $\phi_{\max} = 0.1U_\infty$ over a width of 10° of the jet. They assess various possible configurations by analyzing the impact of the spanwise wavelength of their control λ_z . The difference between both control types is that, while the Out-of-phase has opposed blowing and suction on the top and bottom at the same spanwise location, the In-phase has the same amount of blowing or suction for both surfaces. For a wavelength

of $\lambda_z/D = \pi$ (hence, $\lambda_z/D = L_z$), they reported 18% and 25% drag reduction for the In-phase and Out-of-phase cases, respectively. Since In-phase does not comply with the ZNMF condition, in this study we will consider their Out-of-phase case as the baseline and we will denote it as KC05.

Developing flow-control strategies for fully turbulent 3D wakes around cylinders constitutes a significant challenge for DRL. As the wake becomes three-dimensional, the MARL setup must effectively utilize spanwise characteristic structures to devise efficient control methods, which can have profound implications for drag reduction. Note that DRL can discover new strategies by maximizing rewards R for an agent interacting with the environment through actions A and partial observations S . Through episodes of consecutive actions, neural-network weights are updated, optimizing policies to maximize expected rewards. For recent advances in flow control using MARL, interested readers are directed to Refs. [25–27], where significant progress and insights have been reported.

2 Methodology

This study involves a 3D cylinder subjected to a constant inflow in the streamwise direction, with all lengths non-dimensionalized using the cylinder diameter D . The computational domain, depicted in Figure 1, has dimensions $L_x/D = 40$, $L_y/D = 25$, and $L_z/D = \pi$, with the cylinder centered at $(x/D, y/D) = (12.5, 6.25)$. Here x , y and z denote the streamwise, vertical and spanwise directions, respectively. Note that the coordinate-system origin is located at the front face left-bottom corner. Periodic boundary conditions are used in the cylinder spanwise direction. As discussed in the references presented in Table 1, there is a consensus in the literature that a spanwise length of π is sufficient to statistically capture all wavelengths of the relevant structures. At the inlet, a constant velocity U_∞ is imposed with a Dirichlet condition. The surfaces of the cylinder include the no-slip and no-penetration conditions, while the top, bottom, and outflow surfaces of the domain box are set as zero-stress outlet. The cylinder incorporates two sets of $n_{\text{jet}} = 10$ synthetic jets positioned at the top and bottom surfaces ($\theta_0 = 90^\circ$ or 270° , respectively). Hence, the jet length is $L_{\text{jet}}/D \simeq 0.314$, which is 21.5% shorter than what we employed in previous studies at lower Re_D [17]. This will allow a more flexible strategy when controlling the spanwise structures in the wake, which are finer in the present higher- Re_D case. As discussed in §1, this setup resembles the one reported in Ref. [24], with two differences: first, it will not be a prescribed control (since the DRL framework will enable dynamic changes); and second, the control will change both in the spanwise direction and in time. In the current study, the jet velocity profile in the direction normal to the surface is defined in terms of the angle θ and the desired mass-flow rate per unit length Q as follows:

$$\|U(Q, \theta)\| = Q \frac{\pi}{\rho D \omega} \cos\left(\frac{\pi}{\omega}(\theta - \theta_0)\right), \quad (1)$$

where $Q = \dot{m}/L_z$, $|\theta - \theta_0| \in [-\omega/2, \omega/2]$, \dot{m} is the mass flow rate and ω is the angular opening of the jet as shown in Figure 1. For every pseudo-environment (also called

MARL environment, as discussed later), we set opposite action values between the pair of top and bottom jets, *i.e.* $Q_{90^\circ} = -Q_{270^\circ}$, to guarantee an instantaneous global zero net mass flux, as discussed in Ref. [17].

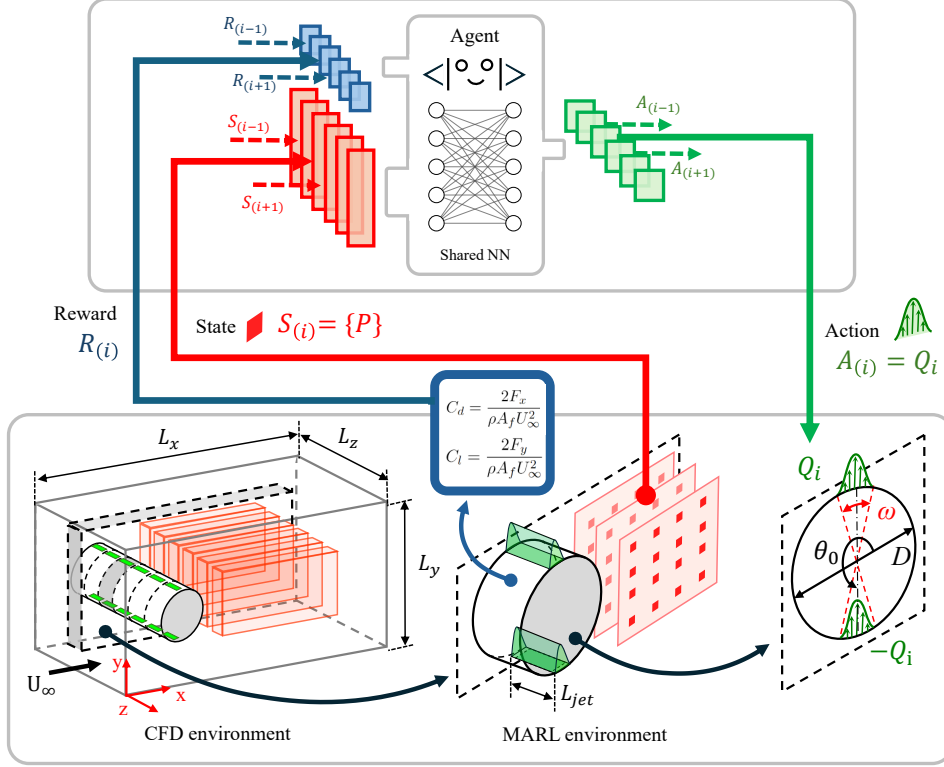


Fig. 1 Schematic representation that illustrates the multi-agent reinforcement-learning framework applied to a three-dimensional cylinder, showcasing communication channels between two main actors. In this case the direction of the information would be clockwise. At the top we show the agent architecture featuring a shared neural network. At the bottom, the computational-fluid-dynamics (CFD) environment featuring a cylinder is depicted, with the cylinder diameter D as the reference length. Moving rightward, emphasis is placed on the local MARL environment, also known as the pseudo-environment. Note that ω represents the jet angle width, while θ_0 denotes the angular location of each jet center. Additionally, the green shading illustrates the sinusoidal velocity profile, which remains uniform in the spanwise direction within a single jet length, L_{jet} .

The numerical simulations are carried out by means of the numerical solver Alya, which is described in detail in Ref. [28]. The spatial discretization is based on the finite-element method (FEM) and the incompressible Navier–Stokes equations, which are formulated below:

$$\partial_t \mathbf{u} + (\mathbf{u} \cdot \nabla) \mathbf{u} - \nabla \cdot (2\nu \boldsymbol{\epsilon}) + \nabla p = \mathbf{f}, \quad (2)$$

$$\nabla \cdot \mathbf{u} = 0, \quad (3)$$

are integrated numerically. Here \mathbf{u} is the velocity vector, $\boldsymbol{\epsilon}$ is the strain-rate tensor $\boldsymbol{\epsilon} = 1/2(\nabla \mathbf{u} + (\nabla \mathbf{u})^T)$ and \mathbf{f} represents external body forces. In equation 2, the convective term $(\mathbf{u} \cdot \nabla) \mathbf{u}$ is formulated to conserve energy, momentum, and angular momentum, as described in Refs. [29, 30]. Time discretization employs a semi-implicit method where the convective term follows a second-order Runge–Kutta scheme, and a Crank–Nicholson scheme is utilized for the diffusive term [31]. Ayla determines the suitable time step using an eigenvalue-based time-integration scheme [32]. Subsequently, the numerical solution of these equations is computed for each time step. Drag and lift forces (F_x and F_y , respectively) are computed through integration over the cylinder surface s :

$$\mathbf{F} = \int (\boldsymbol{\varsigma} \cdot \mathbf{n}) \cdot \mathbf{e}_j ds, \quad (4)$$

where $\boldsymbol{\varsigma}$ is the Cauchy stress tensor, \mathbf{n} the unit vector normal to the surface and \mathbf{e}_j is a unit vector with the direction of the main flow velocity for F_x and the perpendicular cross-flow direction for F_y .

In order to define the uncontrolled case it is important to carefully study the convergence of the cylinder at $Re_D = 3900$. In this study we use a 2D unstructured mesh extruded in the z direction. Following a convergence study, an interval of 300 convective time units, which are defined in terms of U_∞ and D , tU_∞/D , is considered to be sufficiently long to properly capture the pressure distribution around the cylinder, which in turn is associated with the computation of the aerodynamic forces, since the drag of a cylinder in these regimes mostly comes from the pressure component. Our simulations show reasonable agreement with the results reported in the literature for this case, as shown in Table 1. Note that there is some discrepancy in $\overline{C_d}$ (defined later in equation 7 in section §2.1) with the results by Lehmkuhl *et al.* [18], which may be due to mesh resolution or very low-frequency modulations reported in the literature.

2.1 Multi-agent reinforcement learning (MARL)

We implemented a deep-reinforcement-learning (DRL) framework using Tensorforce libraries [36]. DRL is very well suited for unsteady flow-control problems. It provides the possibility to dynamically interact with an environment in a closed-loop approach, being able to set the actuation based on the varying flow state. We use the proximal-policy-optimization (PPO) algorithm [37], which is a policy-gradient approach based on a surrogate loss function for policy updates to prevent drastic drops in performance. This algorithm exhibits robustness, as it is forgiving with hyperparameter initializations and can perform adequately across a diverse range of RL tasks without extensive tuning.

Table 1 The statistical values for flow around a cylinder at $Re_D = 3,900$ are presented, with comparisons made between the results of the present uncontrolled case and results reported in the existing literature.

Reference	L_z/D	St	L_r/D^1	$\overline{C_d}$	$-\overline{C_{pb}}^2$
Present uncontrolled case	π	0.22	1.11	1.08	1.02
Lehmkuhl <i>et al.</i> [18]	π	0.215	1.36	1.015	0.935
Parnaudeau <i>et al.</i> [20]	23	0.208	1.51
Norberg [33] ($Re_D = 3000$)	67	0.22	1.66	0.98	0.88
Lourenco and Shih [34]	21	0.98	0.9
Tremblay <i>et al.</i> [35]	π	0.22	1.3	1.03	0.93
Kravchenko & Moin [22]	π	0.21	1.35	1.04	0.94

¹Recirculation bubble length measured as the distance from the back point of the cylinder to when centerline in x direction velocity is $\bar{u} = 0$.

²Back pressure coefficient defined as $(\bar{p} - p_\infty)/\frac{1}{2}\rho_\infty U_\infty^2$.

The neural-network architecture consists of two dense hidden layers of 512 neurons each. The batch size, *i.e.*, the total number of experiences that the PPO agent utilizes for each gradient-descent iteration, is configured to 60, exceeding the values employed in previous 2D cylinder experiments [38] and previous 3D training scenarios [17]. The main constraint to set such value lies in having 10 actuators per environment, requiring 10 streamed experiences which are synchronized. Thus, we must operate with a total of $10n_{\text{environments}}$ sets of experiences, similar to what has been reported in Ref. [39]. A streamed experience encompasses a collection of states, actions, rewards, and the predicted state that the agent anticipates achieving, denoted as $(S, A, R, S')_{i,t}$ for each pseudo-environment. Moreover, we encounter computational resource limitations. If the batch size is excessively large, a single training session might be interrupted before any batch update occurs, resulting in the loss of cumulative streamed experience.

In previous studies on 2D cylinders, the different training stages were executed using a single-agent reinforcement learning (SARL) setup. However, considering the effectiveness of MARL in managing multiple actuators simultaneously, as demonstrated in recent works [13–15, 17], SARL is not a feasible choice for the current 3D cylinder configuration with distributed input forcing and distributed output reward (referred to as the DIDO scheme). As opposed to SARL, the MARL framework avoids the curse of dimensionality by exploiting invariances and aims to train local pseudo-environments. This approach makes high-dimensional control manageable, as the agents are trained in smaller domains to maximize local rewards. All agents share the same neural-network weights, significantly accelerating training. Each agent is linked to a pair of jets that actuate independently. Observation states S_i comprise partial pressure values along the domain, focused on the wake and near-cylinder regions to exploit the spanwise pressure gradients in the control. As detailed in Table 2, these pressure values form multiple slices in the xy plane, evenly spaced in the spanwise direction. Each set of three slices corresponds to an individual pseudo-environment. The total reward $R(t, i_{\text{jet}})$, as defined in Equation (5), comprises the sum of local, r^{local} , and global, r^{global} , rewards corresponding to each jet i_{jet} . The scalar K_r adjusts the values approximately within the range $[0, 1]$, while β balances the local and global

rewards; in this work, $\beta = 0.8$. The rewards r , defined in Equation (6), are functions of the aerodynamic force coefficients C_d and C_l ($\overline{C_{d_b}}$ represents the averaged value for uncontrolled conditions). The user-defined parameter α serves as a lift penalty, and in our study we set $\alpha = 0.6$. This parameter is crucial for mitigating undesired asymmetric strategies that favor a reduction of the component parallel to the incident velocity (drag) over the perpendicular one (positive or negative lift), commonly known as the axis-switching phenomenon. Note that Table 2 summarizes the rest of MARL and computational-fluid-dynamics (CFD) parameters that define the whole framework employed here.

$$R(t, i_{\text{jet}}) = K_r [\beta r^{\text{local}}(t, i_{\text{jet}}) + (1 - \beta) r^{\text{global}}(t)], \quad (5)$$

$$r(t, i_{\text{jet}}) = \overline{C_{d_b}} - C_d(t, i_{\text{jet}}) - \alpha |C_l(t, i_{\text{jet}})|, \quad (6)$$

$$\text{where } C_d = \frac{2F_x}{\rho A_f U_\infty^2} \quad \text{and} \quad C_l = \frac{2F_y}{\rho A_f U_\infty^2}. \quad (7)$$

The aerodynamic forces described in Equation (7) incorporate the frontal area $A_f = DL_{\text{jet}}$, derived from the local pseudo-environment surfaces for C_d^{local} , and from the entire cylinder for C_d^{global} .

The interactions between the agent and the physical environment are represented by actions A , which influence the system over an interval of T_a time units. We update the jet boundary conditions using Equation (1). To transition smoothly between the actions at times t and $t + 1$, $Q_t \rightarrow Q_{t+1}$, we employ exponential functions. This ensures a gradual shift in time, reducing the occurrence of sudden mass discontinuities that could disrupt the training process. The DRL library requires rescaling such that $Q = AQ_{\text{max}}$ to prevent excessively large actuations. Accordingly, $Q_{\text{max}} = 0.176$ was determined based on our experience with DRL for flow control in Refs. [17, 38].

The episode duration is specifically set to span at least seven vortex-shedding periods ($T_{\text{vs}} = 1/f_{\text{vs}}$). We choose $T_a \approx 0.05T_{\text{vs}}$, based on insights gained from previous studies [40]. A vortex-shedding period is $T_{\text{vs}} = 1/St \approx 4.7$, based on the existing literature. Note that $St = f_{\text{vs}}D/U_\infty$ is the Strouhal number, and f_{vs} denotes the vortex-shedding frequency. This interval allows sufficient time between actions to produce an effect on the flow. A shorter T_a could introduce noise into the training process, complicating trajectory exploration and correlation. Conversely, an excessively long T_a may compromise the capability of the agent to control shorter characteristic time scales. Thus, a total of 150 actuations per episode is deemed adequate for evaluating cumulative rewards.

Each episode commences from an uncontrolled converged state of the problem, also called baseline. Hence, each episode continues the simulation from the last baseline timestep. Additionally, we compare our DRL-based control, from now on called DRL-10, with the control based on the Kim & Choi Out-of-phase setup, denoted in this work as KC05.

Table 2 Main parameters of the MARL architecture and the CFD setup used in the present work, for the DRL-10 case.

Parameter	Value/type
Number of grid points	9.6 million
L_x/D	40
L_y/D	25
L_z/D	π
L_{jet}/D	0.314
S	183 (3 xy slices of 61)
Variable used for S	Pressure
Q_{max}	0.176
K_r	5
α	0.6
β	0.8
T_a	0.25
Actions/episode	150
CPUs/environment	1800
Parallel CFD environments	6
Actuators/CFD environment	10
Batch size	60
Baseline duration [D/U_∞]	300
Neurons (hidden layers)	512 (2)
Time-smoothing function	Exponential

3 Results

In this section we present the successful training at $Re_D = 3900$ which rely on a MARL implementation. The training process, associated challenges, the convergence assessment through reward evaluation and its contributions will be described initially. Subsequently, the model will be evaluated using the agent already trained in exploitation mode, also known as deterministic mode. The latter entails choosing actions without exploration; the agent solely applies the action associated with the highest probability of maximal reward given a particular state. Statistical results are presented alongside the uncontrolled case and the controlled reference case KC05. The purpose of conducting such a comparison is to clarify which drag-reduction physical mechanisms are being explored by the agent.

3.1 Exploration

Setting up a good training configuration in advance is crucial for achieving a consistent and efficient reward improvement. In fact, it is worth noting that to reach the configuration already shown in Table 2, there has been an iterative process of trying different values of the main parameters. For instance, unsuccessful attempts were made with an observation state of $S = 181 \times 3$ slices (543 pressure values in total) or with $n_{\text{jet}} = 15$, hence $L_{\text{jet}}/D \simeq 0.21$. DRL requires methodical hyperparameter tuning in order to obtain the optimal parameters for the case under study.

The exploration is evaluated continuously by monitoring the final and cumulative rewards in real time. Based on our experience, the most helpful metrics to track are

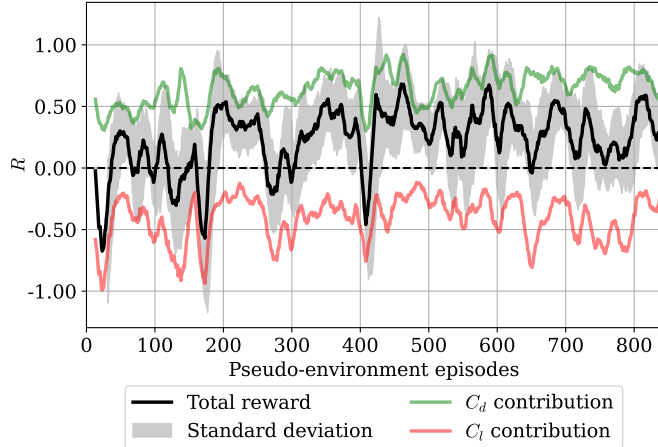


Fig. 2 Evolution of the rewards at the end of each pseudo-environment episodes, denoted as R , throughout the exploration phase, along with its contributions from lift-bias and pure drag-reduction during training sessions. The signals are smoothed using a moving average of 15 values.

the total reward, its contribution due to lift-bias, $-\alpha|C_l(t, i_{jet})|$, and the pure drag reduction, $C_d - \overline{C_{d_b}}$. The Figure 2 shows the difficulties when assessing whether a particular training is converged. In this example, despite the fact that the C_d reduction converges to an acceptable value of the reward, the maximum/minimum and standard deviation characterize the magnitude of the oscillations, which can be detrimental for the learning process. To further assess the learning, an intermediate exploitation of the model is also needed to monitor the drag reduction and if the control strategies are depicting any pattern. Based on our experience, this is very important when tackling such unsteady and chaotic environments. After around 500 pseudo-environment episodes we observe how the C_d reduction is maintained without significant minima. This signifies how the exploration is already testing trajectories on the right path and has already discarded some of them that clearly lead to undesired outcomes, aiming to maximize rewards.

In terms of computational expense, training constitutes the dominant part. The presented training session required 840 trajectories, akin to executing 84 numerical simulations with 10 pseudo-environments each. All exploration sessions were conducted on the Dardel high-performance-computing (HPC) in the PDC Center, KTH Royal Institute of Technology. These sessions operate across 90 nodes concurrently, each 15 nodes executing a single numerical simulation consisting of 10 simultaneous pseudo-environments, totaling 60 pseudo-environments. Each node is equipped with two AMD EPYC™ Zen2 2.25 GHz 64-core processors and 512 GB of memory. With each batch of 6 CFD simulations optimally requiring approximately 10 hours in this specific architecture, the process involves a minimum of one week of continuous operation. This is equivalent to using 11,520 CPU cores running for $\simeq 2$ million CPU hours in total. It should be noted that making an accurate estimation for such training session is difficult, considering synchronization times, the necessary restarts

between episodes, and data movement in memory and on disk. After deciding to conclude the exploration phase, we proceed to evaluate the deployment of the model and its performance during exploitation.

3.2 Exploitation

When the agent operates without exploration, it selects the best possible action using the probability distribution that has obtained during the learning process. In Figure 3 we show how drag is reduced during exploitation, comparing the results of DRL-10 with those of KC05 and the uncontrolled case. The effectiveness of the KC05 strategy is evident, but as will be discussed later, it requires significantly higher actuation cost. Focusing on DRL-10, we observe a clear tendency to reduce C_d , although the flow experiences very low-frequency oscillations, with a period of approximately 40 time units. Although at times DRL-10 improves upon the KC05 values, the minimal oscillations of the latter show better consistency in the control.

Another important aspect to emphasize is the transition stage once the control is activated. In the Figure 3 it can also be observed that the KC05 case takes about 40 time units before stabilizing on a value of C_d . On the other hand, DRL-10 is able to act more quickly; it reaches the minimum drag it can achieve in half the time but fails to stabilize and gives way to the aforementioned low-frequency modulation. This may be due to the design of the training; starting all episodes from the same point seems insufficient to explore control space for stabilizing those minimum environment values of $C_d = 0.92$.

Table 3 shows the most relevant physical quantities values taking into account aerodynamic forces. All values are averaged over the last 100 time units in the converged stage, equivalent to ≈ 20 shedding periods. We observe how the DRL-10 case is able to influence the St number, while the KC05 case has no influence in that sense. The drag-reduction mechanism is very similar to those reported in Refs. [17, 38], at least statistically. Interestingly, the recirculation bubble is extended by 45% in DRL-10 and by 71% in KC05 relatively to the case without control. The pressure valley at the most downstream point increases slightly, a fact that is directly related to the integral necessary for computing the forces exerted on the surfaces.

The aspect in which DRL-10 significantly outperforms KC05 is in the mass cost associated with the control. Only considering the maximum values of mass-flow rate per unit length over time, it can be observed that it is an order of lower magnitude in the DRL-10 case. But if we also consider that KC05 maintains a constant value over time instead of fluctuating like DRL-10, we observe $E_c^*/\Delta C_d$ ratios two orders of magnitudes lower. Note that E_c^* is defined as:

$$E_c^* = \frac{E_c}{E_\infty} = \frac{L_{\text{jet}}}{(t_2 - t_1)Q_\infty L_z} \int_{t_1}^{t_2} \sum_{i=1}^{n_{\text{jets}}} |Q_i(t)| dt, \quad (8)$$

which represents the mass cost over time of any control system with n_{jets} compared to the corresponding mass intercepted by the cylinder E_∞ , where $Q_\infty = DU_\infty$. Note that low values of $E_c^*/\Delta C_d$ imply that control is much more efficient in terms of used

mass per drag reduction ΔC_d . Regarding the fluctuations indicated by the root-mean-squared values of C_d and C_l , they are very small for the KC05 case, exhibiting a behavior similar to those in previous cases studied in the transition regimes between $Re_D = 100$ to 400. The actuation is robust and able to remain stable once it reaches the minimum. On the other hand, DRL-10 experiences difficulties and is not as effective in that sense, particularly when it comes to the vertical forces. On the one hand, DRL-10 yields 8.3% reduction, while KC05 produces 14.7% reduction (which is lower than the 18% reported in the original study [24]). On the other hand, the ratio $E_c^*/\Delta C_d$ is 0.0014 in DRL-10 and 0.22 in KC05, *i.e.* the DRL-10 case is two orders of magnitude more efficient in terms of mass-flow rate usage normalized by the amount of drag reduction obtained. This is due to the fact that the DRL control is much more nuanced than the fixed spanwise control by KC05, and is able to adapt to the instantaneous state of the wake, effectively exploiting the wake structures to achieve drag reduction. Note that in Table 3 we also include the main frequency of the mass-flow control signal, denoted as f_c . It is interesting to note that this frequency is completely different from the uncontrolled Strouhal number or the modified Strouhal number in the controlled case.

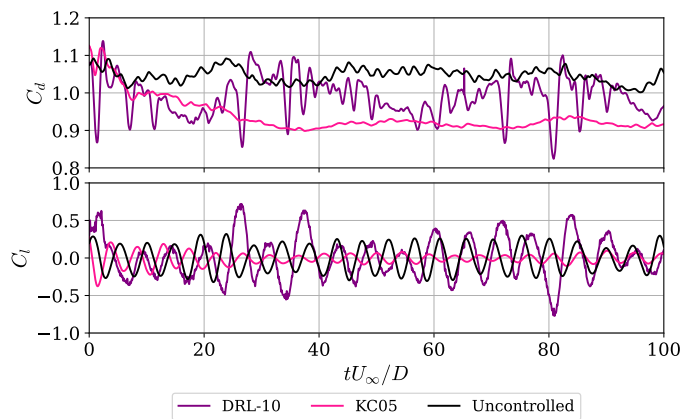


Fig. 3 Evolution in time of the (top) drag coefficient C_d and (bottom) lift coefficient C_l . Note that the transitional stage is included. When $tU_\infty/D = 0$ the control starts for both cases, DRL-10 and KC05.

To study how the wake topology changes in the various scenarios, we show the vortical motions in the instantaneous flow in Figure 4. The most remarkable aspect is the non-invasive character of DRL-10 compared to KC05, where there is clearly a peak of suction and another one of blowing for the latter. This is particularly evident in the Kelvin–Helmholtz instabilities, clearly represented by the smaller structures at the top with high values of streamwise velocity. Both controls appear to extend the duration of these instabilities, thereby increasing the recirculation bubble. Also note that both controls delay the baseline location of the vortex shedding.

Table 3 Summary of the main characteristics for both controlled cases compared with the present uncontrolled case. All values are averaged over 100 time units after discarding the initial transients resulting after applying the control.

	Uncontrolled	DRL-10	KC05
St	0.22	0.177	0.22
L_r/D Bubble length	1.11	1.61	1.9
$-C_{pb}$	-1.02	-0.81	-0.76
Q_{\max}	...	0.053	0.11
Q_{RMS}	...	0.037	...
f_c	...	0.115	...
C_d	1.08	0.99	0.921
$C_{d_{\text{RMS}}}$	0.021	0.049	0.015
$C_{I_{\text{RMS}}}$	0.236	0.29	0.044
ΔC_d [%]	...	-8.33	-14.7
$E_c^*/\Delta C_d$...	0.0014	0.22

Figure 5a illustrates the benefits offered by a system like MARL. In comparison to what is observed at lower Reynolds numbers [17], where it was clear that the control tries to synchronize all jets to act at the same frequency, here we have a much richer control. As shown by the power-spectral density in Figure 5b, Q evolution in DRL-10 exhibits more features besides the main frequency f_c . In contrast, strategy reported for $Re_D = 400$ in Ref. [17] only has a clear peak and a second harmonic compared to the rest of its spectrum. It can be observed a control resolution where multiple actuators collaborate. Among them, they form a distributed blowing/suction spanning a spanwise length of around D , which aligns with the wavelengths experienced in this classic fluid case.

As a general observation, building on the previous discussion about mass cost, it is worth noting that in the DRL-10 strategy the values are mainly within the range $Q_{\text{DRL-10}} = \pm 0.01$, which is ten times less than Q_{KC05} . The equivalent mass-flow per unit length for KC05 is $Q_{\text{KC05}} = 0.11$. Despite this observation, there are some occasional and short peaks in $Q_{\text{DRL-10}}$ that saturate the signal, reaching $Q_{\text{DRL-10}} > 0.02$, which indicates that the DRL-10 controller is able to exploit the full mass flow rate authority that is provided to it, when needed. Overall, it is important to highlight that despite the agent being able to explore beyond this range during training, it decides to limit the maximum values by only a $10\%Q_{\max}$ during exploitation. This indicates that the algorithm tends to be conservative and adheres to an efficiency guideline, aiming to utilize the minimum mass-flow rate that maximizes the desired impact. Actually, in our experience, in this particular application a lack of learning signal is often indicated by sudden signal saturation, when the agent trajectory is not performing well and loses its ability to handle the actual flow situation.

This sophisticated distribution is remarkable if we focus on the standard deviation σ shown in Figure 5b, orders of magnitude higher than the reference case of $Re_D = 400$ in Ref.[17]. The agent at $Re_D = 3900$ is capable of acting precisely on the dominant structures in the wake, which exhibit a rich range of frequencies in the spanwise direction.

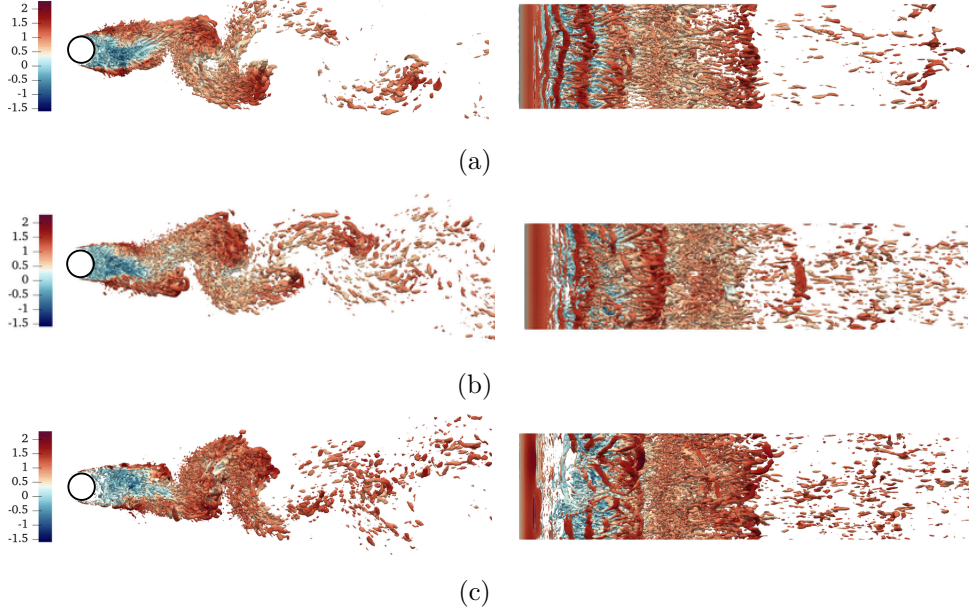


Fig. 4 Instantaneous coherent structures identified with the λ_2 criterion [41], where the isosurfaces $\lambda_2 D^2/U_\infty^2 = -5$ are coloured by the streamwise velocity. We show (a) uncontrolled, (b) DRL-10 and (c) KC05 cases, and all of them are chosen to show the flow in a statistically converged stage.

Next, we study the spectra of temporal signals of the streamwise and cross-flow velocities for two locations in the wake of the cylinder, see Figure 6. Inspired by the study conducted by Lehmkühl *et al.* [18], points P1 at $(x/D, y/D, z/D) = (6.81, 13.25, 1.26)$ and P2 at $(x/D, y/D, z/D) = (8.25, 13.25, 1.26)$ were chosen to assess the main frequencies and compare them with those reported in the literature.

In the uncontrolled case, the shedding frequency of vortices $f_{vs} = 0.22$ is clearly captured at both locations. However, at the P1 location, it seems to be too close to the cylinder surface to effectively capture the bubble instability, especially when considering the streamwise velocity. Additionally, at point P2, we can discern the emergence of a higher frequency at $f_{KH} = 1.55$, which according to literature, could be associated with the Kelvin–Helmholtz instability in the separating shear layer. The observed value is slightly higher than the estimate provided by Prasad and Williamson [42], which is given as $f_{KH} = 0.0235 Re_D^{0.67} f_{vs} = 1.31$.

If we compare with the results of the controlled cases, we can observe the influence of the actuators in both DRL-10 and KC05. For the first one, there is a shift to a lower shedding frequency and lower intensity, $f_{vs}^{DRL-10} = 0.177$. Meanwhile, KC05 maintains the same shedding frequency, $f_{vs}^{KC05} = f_{vs} = 0.22$, but with a slight decrease in intensity. This is consistent with the fact that the KC05 control does not involve any temporal dependency, thus not affecting the dominant frequency in the wake. At point P1 (Figure 6), it is interesting how the intensity of the energy cascade for KC05 is much lower compared with to the uncontrolled case, while DRL-10 exhibits

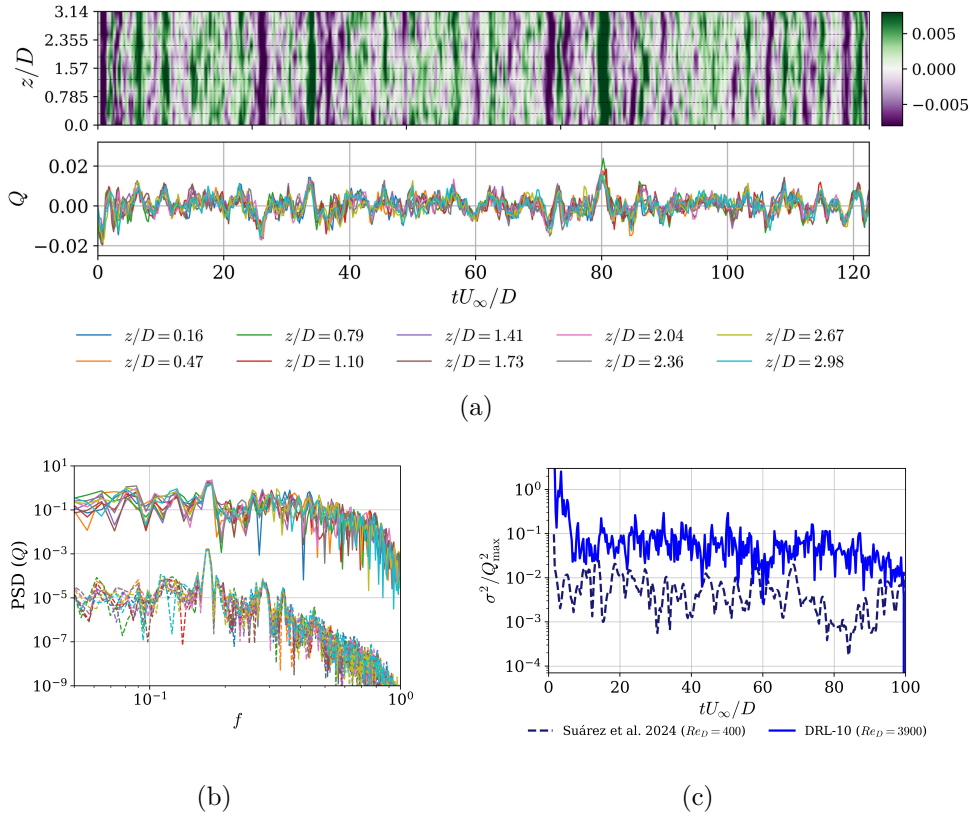


Fig. 5 (a) Mass-flow rate per unit width Q as a function of time for all jets, showing (top) spatial distribution over z/D and (bottom) individual evolutions of the various jets. (b) Power-spectral density of all actuators Q signals in time comparing (solid shifted by 10^2) present study DRL-10 at $Re_D = 3900$ and (dashed) for $Re_D = 400$ reported in Ref. [17]. (c) Evolution in time of the variance of the mass-flow rate computed in z , $\sigma^2(t) = (1/n_{\text{jets}}) \sum_{i=1}^{n_{\text{jets}}} (Q_i(t) - \bar{Q}(t))^2$, and normalized by the squared peak Q values from each case. Note that this trend is compared with the $Re_D = 400$ case extracted from previous work done in Ref. [17].

a slight increase. It can be inferred that the agent is enriching the finer scales near the cylinder, whereas the strong actuation of KC05 causes such structures to fade.

The influence of the studied AFC is not limited to frequencies but also extends to the mean fields in the wake. First, Figure 7a shows how the recirculation bubble is enlarged as a result of both controls. In the DRL-10 case, we can observe a shorter recirculation bubble than in the KC05 case, also exhibiting fewer regions of mean streamwise velocity where $|\bar{u}| < 0.03$ (highlighted as yellow-colored regions). The KC05 case resembles the uncontrolled configuration, with larger regions of zero velocity than the DRL-10 case. Second, in Figure 7b and Figure 7c we analyze the Reynolds stresses. We observe a similar trend in both cases, DRL-10 and KC05, where the maximum stresses are reduced by $\approx 50\%$ and their locations shifted backwards an

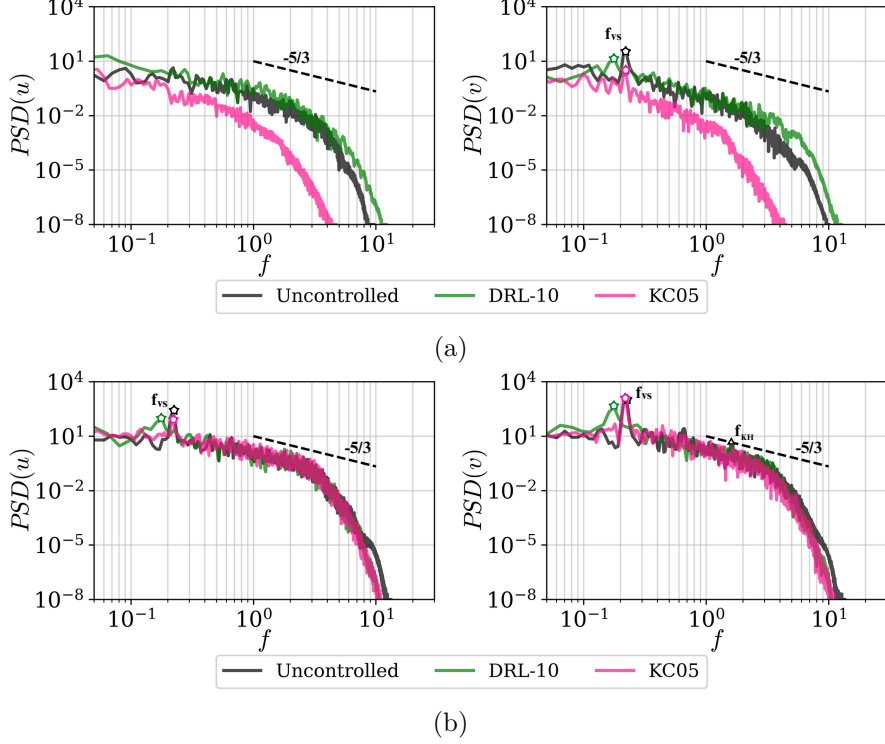


Fig. 6 Power-spectral density of the (left) streamwise u and (right) cross-stream v velocities. We consider the points located at coordinates: (a) P1, $(x/D, y/D, z/D) = (6.81, 13.25, 1.26)$ and (b) P2, $(x/D, y/D, z/D) = (8.25, 13.25, 1.26)$. Three cases are shown, and the main frequencies are denoted by f_{vs} for vortex shedding and f_{KH} for Kelvin–Helmholtz instabilities. We also include a dashed line showing the $k = -5/3$ spectrum.

approximate length of D . This behavior is consistent with drag-reduction mechanisms observed at lower-Reynolds-number [17].

The pressure distribution on the surface of the cylinder is shown to be consistent with the literature, except for a slight deviation in the minimum peak at $\theta \approx -112.5^\circ$, as seen in the Figure 8a. However, when considering the influence of the control, we observe that the most significant change is in the distribution precisely within the separation bubble delimited by $\pm\theta_s \approx 89^\circ$.

On the other hand, we observe a V-shaped mean streamwise velocity along the centerline in the wake. This shows good agreement with the literature. This observation is related with the phase shift discussed above. The reattachment with the downstream velocity value occurs approximately $1D$ later, for both DRL-10 and KC05. The former reaches to reach higher negative velocity values, while KC05 is better at maintaining more regions around $\bar{u} = 0$ near the cylinder.

To conclude the analysis, the different velocity profiles along the wake show very good agreement with the literature, see Figure 9. Given that significant scattering with the references typically happens near the cylinder, the observations at the first

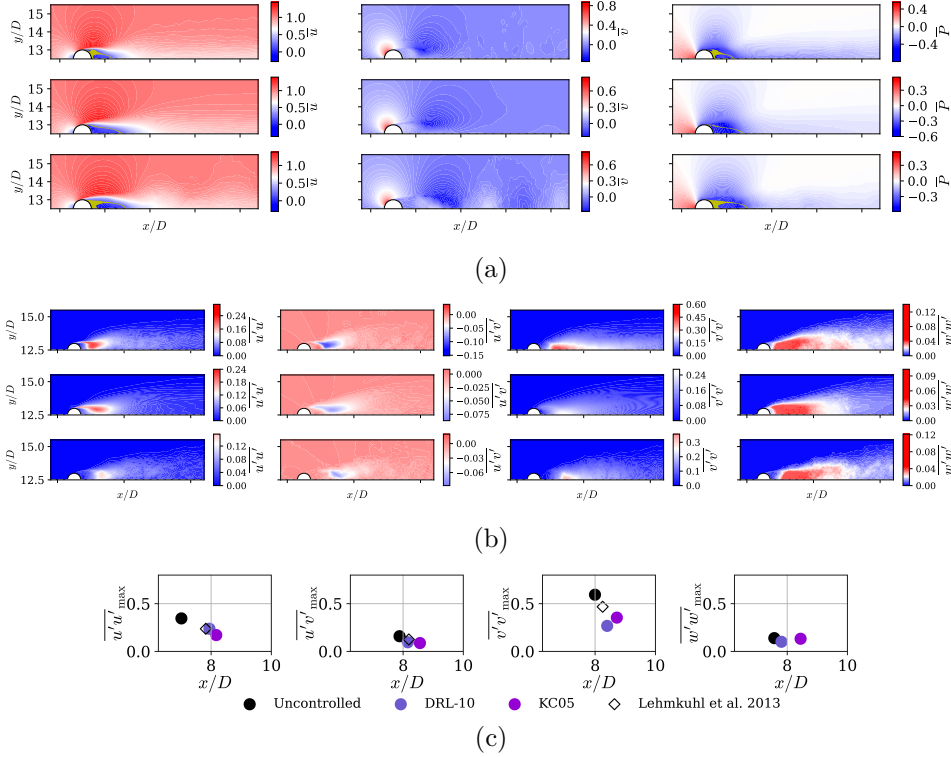


Fig. 7 Time- and spanwise-averaged flow-field statistics comparison. (a) Mean velocities, \bar{u} and \bar{v} , and mean pressure \bar{p} fields for (top) uncontrolled, (middle) DRL-10 and (bottom) KC05. Yellow regions denote wake-stagnation points where $|\bar{u}| < 0.03$, which is used to compute L_r/D in Table 3. (b) Mean Reynolds stresses $\overline{u'u'}$, $\overline{u'v'}$, $\overline{v'v'}$ and $\overline{w'w'}$ for (top) uncontrolled, (middle) DRL-10 and (bottom) KC05. (c) Maximum Reynolds-stress values and their corresponding x/D locations across all investigated cases, compared with values from the literature [18].

three locations ($x/D = 6.83, 7.31$, and 7.79) reaffirm our earlier observations: the recirculation zone is wider in both controlled cases. Additionally, \bar{u} exhibits a flatter shape near the centerline. For instance, focusing on $x/D = 7.79$, It is noteworthy how the recirculation is maintained, while the uncontrolled case, \bar{u} reattaches to the downstream velocity further into the wake. As expected, far from the cylinder, the wake recovers its shape similarly for all cases, there is no significant influence due to control mechanisms here.

4 Conclusion

This study couples a multi-agent reinforcement learning (MARL) framework with a numerical solver to explore efficient drag-reduction strategies by controlling multiple jets positioned along the span of a three-dimensional cylinder. The investigation is conducted at $Re_D = 3900$, representing the fully turbulent wake, and compared with

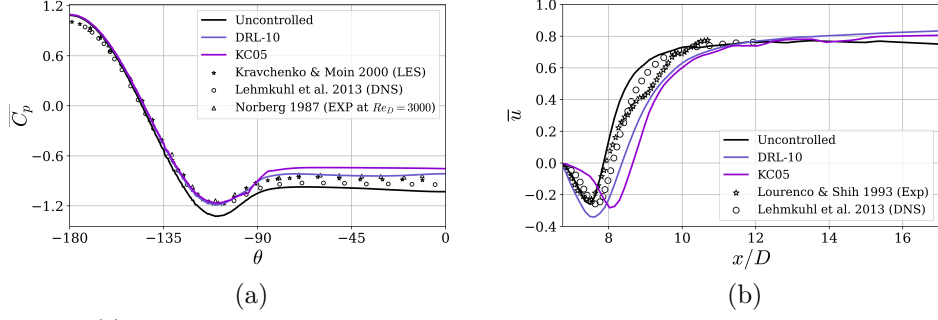


Fig. 8 (a) Pressure-coefficient distribution around the cylinder, where $\theta = 0$ is the back of the cylinder. (b) Averaged streamwise velocity along the centerline at $y/D = L_y/2$. Note that several curves from the literature are included to validate the present uncontrolled case in all figures.

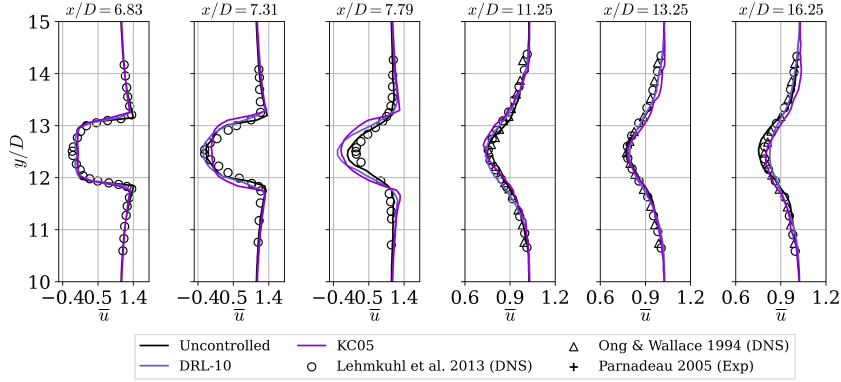


Fig. 9 Mean streamwise velocity \bar{u} profiles at different locations along the wake. Note that reference trends from the literature are included to validate the present uncontrolled case in all the figures.

a classical case referred to as KC05, based on the Out-of-phase strategy reported by Kim & Choi [24]. The DRL-based control policy outperforms by two orders of magnitude the ratio of mass cost per $\Delta \overline{C_d}$ used in the KC05 strategy. The DRL-based control strategy exploits the emergence of spanwise instabilities to discover drag-reduction strategies. This is done by leveraging the underlying physics within pseudo-environments and optimizing the global problem involving multiple interactions concurrently. These findings showcase the effectiveness of the DRL approach, which has the ability to identify flow-control strategies more sophisticated than those obtained with classical control, covering a wide range of possible frequencies to control and addressing various flow-structure wavelengths appearing in the wake. An advantage of MARL is its ability to deploy trained agents across various cylinder lengths and numbers of actuators while ensuring consistency in the spanwise width of the jets and their corresponding pressure values as observation states. It is worth noting that the training focuses on symmetries and invariant structures, a task not feasible with

SARL due to its limitations. MARL enables cost-effective training sessions in smaller, simplified computational domains, thereby accelerating the process required for flow control in high-fidelity simulations.

The current DRL-based control strategy demonstrates a significant reduction in drag, *i.e.* 8%. Moreover, it is important to note that this study marks a pioneering training process conducted in fully turbulent 3D cylinders at $Re_D = 3900$ within the framework of MARL implementation. This achievement sets a new benchmark for the DRL community and holds the potential to inspire its adoption in future distributed-input distributed-output schemes.

Declarations

Funding

This study was enabled by resources provided by the National Academic Infrastructure for Supercomputing in Sweden (NAISS) at PDC, KTH Royal Institute of Technology. R.V. acknowledges financial support from ERC grant no.2021-CoG-101043998, DEEPCONTROL. Views and opinions expressed are however those of the author(s) only and do not necessarily reflect those of the European Union or the European Research Council. Neither the European Union nor the granting authority can be held responsible for them.

Conflict of interest

The authors have no conflicts to disclose.

Ethical approval

Not applicable.

Informed consent

Not applicable.

Authors' contributions

Suárez, P.: Methodology, software, validation, investigation, writing - original draft and visualization. **Álcantara-Ávila, F., Rabault, J., Miró, A. & Font, B. :** Methodology, software, and writing - review & editing. **Lehmkuhl, O. :** Funding acquisition, supervision, and writing - review & editing. **Vinuesa, R.:** Conceptualization, project definition, methodology, resources, writing - original draft, supervision, project administration and funding acquisition.

Data availability statement

The data presented in this study are available upon request from the corresponding author.

References

- [1] Choi, H., Jeon, W.-P. & Kim, J. Control of flow over a bluff body. *Annual Review of Fluid Mechanics* **40**, 113–139 (2008).
- [2] Vinuesa, R., Brunton, S. L. & McKeon, B. J. The transformative potential of machine learning for experiments in fluid mechanics. *Nature Reviews Physics* **5**, 536–545 (2023).
- [3] Le Clainche, S. *et al.* Improving aircraft performance using machine learning: A review. *Aerospace Science and Technology* **138** (2023).
- [4] Silver, D. *et al.* Mastering the game of go with deep neural networks and tree search. *Nature* **529**, 484–503 (2016).
- [5] Ibarz, J. *et al.* How to train your robot with deep reinforcement learning: lessons we have learned. *The International Journal of Robotics Research* **40**, 698–721 (2021).
- [6] Tang, H., Rabault, J., Kuhnle, A., Wang, Y. & Wang, T. Robust active flow control over a range of Reynolds numbers using an artificial neural network trained through deep reinforcement learning. *Physics of Fluids* **32** (2020).
- [7] Li, J. & Zhang, M. Reinforcement-learning-based control of confined cylinder wakes with stability analyses. *Journal of Fluid Mechanics* **932**, A44 (2022).
- [8] Ren, F., Rabault, J. & Tang, H. Applying deep reinforcement learning to active flow control in weakly turbulent conditions. *Physics of Fluids* **33** (2021).
- [9] Chatzimanolakis, M., Weber, P. & Koumoutsakos, P. Learning in two dimensions and controlling in three: Generalizable drag reduction strategies for flows past circular cylinders through deep reinforcement learning. *Phys. Rev. Fluids* **9**, 043902 (2024).
- [10] Yan, L. *et al.* Stabilizing the square cylinder wake using deep reinforcement learning for different jet locations. *Physics of Fluids* **35**, 115104 (2023).
- [11] Chen, W., Wang, Q., Yan, L., Hu, G. & Noack, B. R. Deep reinforcement learning-based active flow control of vortex-induced vibration of a square cylinder. *Physics of Fluids* **35** (2023).
- [12] Vinuesa, R., Lehmkuhl, O., Lozano-Durán, A. & Rabault, J. Flow control in wings and discovery of novel approaches via deep reinforcement learning. *Fluids* **7**, 62 (2022).
- [13] Font, B., Alcántara-Ávila, F., Rabault, J., Vinuesa, R. & Lehmkuhl, O. Active flow control of a turbulent separation bubble through deep reinforcement learning. *Journal of Physics: Conference Series* **2753**, 012022 (2024).

- [14] Guastoni, L., Rabault, J., Schlatter, P., Azizpour, H. & Vinuesa, R. Deep reinforcement learning for turbulent drag reduction in channel flows. *European Physical Journal E* **46**, 27 (2023).
- [15] Vignon, C. *et al.* Effective control of two-dimensional Rayleigh–Bénard convection: invariant multi-agent reinforcement learning is all you need. *Physics of Fluids* **35** (2023).
- [16] Wang, Z., Fan, D., Jiang, X., Triantafyllou, M. S. & Karniadakis, G. E. Deep reinforcement transfer learning of active control for bluff body flows at high reynolds number. *Journal of Fluid Mechanics* **973**, A32 (2023).
- [17] Suárez, P. *et al.* Active flow control for three-dimensional cylinders through deep reinforcement learning. *14th International ERCOFTAC Symposium on Engineering, Turbulence, Modelling and Measurements: 6th-8th September 2023, Barcelona, Spain: proceedings. Preprint arXiv: 2309.02462* (2023).
- [18] Lehmkuhl, O., Rodríguez, I., Borrell, R. & Oliva, A. Low-frequency unsteadiness in the vortex formation region of a circular cylinder. *Physics of Fluids* **25** (2013).
- [19] Norberg, C. An experimental investigation of the flow around a circular cylinder: influence of aspect ratio. *Journal of Fluid Mechanics* **258**, 287–316 (1994).
- [20] Parnaudeau, P., Carlier, J., Heitz, D. & Lamballais, E. Experimental and numerical studies of the flow over a circular cylinder at Reynolds number 3900. *Physics of fluids* **20** (2008).
- [21] Ma, X., Karamanos, G. S. & Karniadakis, G. E. Dynamics and low-dimensionality of a turbulent near wake. *Journal of Fluid Mechanics* **410**, 29–65 (2000).
- [22] Kravchenko, A. G. & Moin, P. Numerical studies of flow over a circular cylinder at $Re_D=3900$. *Physics of Fluids* **12**, 403–417 (2000).
- [23] Franke, J. & Frank, W. Large eddy simulation of the flow past a circular cylinder at $Re_D=3900$. *Journal of Wind Engineering and Industrial Aerodynamics* **90**, 1191–1206 (2002). 3rd European-African Conference on Wind Engineering.
- [24] Kim, J. & Choi, H. Distributed forcing of flow over a circular cylinder. *Physics of Fluids* **17**, 033103 (2005).
- [25] Belus, V. *et al.* Exploiting locality and translational invariance to design effective deep reinforcement learning control of the 1-dimensional unstable falling liquid film. *AIP Advances* **9** (2019).
- [26] Brunton, S. L. & Noack, B. R. Closed-Loop Turbulence Control: Progress and Challenges. *Applied Mechanics Reviews* **67** (2015).

- [27] Vignon, C., Rabault, J. & Vinuesa, R. Recent advances in applying deep reinforcement learning for flow control: Perspectives and future directions. *Physics of Fluids* **35** (2023).
- [28] Vázquez, M. *et al.* Alya: Multiphysics engineering simulation toward exascale. *Journal of Computational Science* **14**, 15–27 (2016).
- [29] Charnyi, S., Heister, T., Olshanskii, M. A. & Rebholz, L. G. On conservation laws of navier–stokes galerkin discretizations. *Journal of Computational Physics* **337**, 289–308 (2017).
- [30] Charnyi, S., Heister, T., Olshanskii, M. A. & Rebholz, L. G. Efficient discretizations for the EMAC formulation of the incompressible Navier–Stokes equations. *Applied Numerical Mathematics* **141**, 220–233 (2019).
- [31] Crank, J. & Nicolson, P. A practical method for numerical evaluation of solutions of partial differential equations of the heat-conduction type. *Mathematical proceedings of the Cambridge philosophical society* **43**, 50–67 (1947).
- [32] Trias, F. & Lehmkuhl, O. A self-adaptive strategy for the time integration of Navier-Stokes equations. *Numerical Heat Transfer Part B: Fundamentals*, 116–134 (2011).
- [33] Norberg, C. Ldv-measurements in the near wake of a circular cylinder. *ASME paper no. FEDSM98-521* **41** (1998).
- [34] Lourenço, L. M. & Shih, C. Characteristics of the plane turbulent near wake of a circular cylinder. *Published in Ref.[43]* (1993).
- [35] Tremblay, F., Manhart, M. & Friedrich, R. LES of flow around a circular cylinder at a subcritical reynolds number with cartesian grids. *Advances in LES of Complex Flows* 133–150 (2002).
- [36] Schaarschmidt, M., Kuhnle, A. & Fricke, K. TensorForce: A TensorFlow library for applied reinforcement learning (2017). URL <https://github.com/reinforceio/tensorforce>. Published: Web page.
- [37] Schulman, J., Wolski, F., Dhariwal, P., Radford, A. & Klimov, O. Proximal policy optimization algorithms (2017). [1707.06347](https://arxiv.org/abs/1707.06347).
- [38] Varela, P. *et al.* Deep reinforcement learning for flow control exploits different physics for increasing Reynolds number regimes. *Actuators* **11**, 359 (2022).
- [39] Rabault, J. & Kuhnle, A. Accelerating deep reinforcement learning strategies of flow control through a multi-environment approach. *Physics of Fluids* **31** (2019).
- [40] Rabault, J., Kuchta, M., Jensen, A., Reglade, U. & Cerardi, N. Artificial Neural Networks trained through Deep Reinforcement Learning discover control

- strategies for active flow control. *Journal of Fluid Mechanics* **865**, 281–302 (2019).
- [41] Jeong, J. & Hussain, F. On the identification of a vortex. *Journal of Fluid Mechanics* **285**, 69–94 (1995).
- [42] Prasad, A. & Williamson, C. H. K. The instability of the shear layer separating from a bluff body. *Journal of Fluid Mechanics* **333**, 375–402 (1997).
- [43] Beaudan, P. B. *Numerical experiments on the flow past a circular cylinder at sub-critical Reynolds number* (Stanford University, 1995).